PHOTONICS Research

Synergistically modulated $CsPbBr_3$/graphene photoelectric synapses for enhanced image recognition performance

Xiaoying He,[1,5] Haoran Yong,[1] Yunxia Hu,[2,3] Bing Duan,[1] Minhao Xu,[1] Yuxiang Li,[2,3] Bolun Zhang,[4] Yemei Wang,[4] Lan Rao,[1] Qiaoli Liu,[1] Nan Zhang,[2,3,6] and Daquan Yang[1,4,*]

[1]State Key Laboratory of Information Photonics and Optical Communications and School of Electronic Engineering, Beijing University of Posts and Telecommunications, Beijing 100876, China

[2]Beijing Engineering Research Center of Mixed Reality and Advanced Display, School of Optics and Photonics, Beijing Institute of Technology, Beijing 100081, China

[3]Key Laboratory of Photoelectronic Imaging Technology and System, Ministry of Education, Beijing Institute of Technology, Beijing 100081, China

[4]State Key Laboratory of Information Photonics and Optical Communications and School of Information and Communication Engineering, Beijing University of Posts and Telecommunications, Beijing 100876, China

[5]e-mail: xiaoyinghe@bupt.edu.cn

[6]e-mail: nanzhang@bit.edu.cn

*Corresponding author: ydq@bupt.edu.cn

Received 10 April 2026; revised 31 May 2026; accepted 4 June 2026; posted 8 June 2026 (Doc. ID 601313); published 27 July 2026

Perovskite-based synapses are regarded as promising candidates for mitigating the von Neumann bottleneck and advancing the field of visual bionics. However, they suffer performance degradation under long-term environmental exposure. Thus, developing a performance-oriented restoration strategy is essential to realize their practical potential. Herein, we fabricate an ion-gel-gated $CsPbBr_3$/graphene synaptic device in which the perovskite is pre-treated with $TFSI^-$ anions to delay performance degradation. After one year tracing in natural conditions, the recognition accuracy declined from 96.13% to 67.8%. To address this, we propose a photoelectronic synergistic modulation strategy to restore performance. By fine-tuning the gate voltage from 5 mV to 10 mV, the photocurrent increases by ~34.8%, reaching ~3.43 μA, and the recognition accuracy is restored to approximately 93.01%, close to its initial level. This approach enhances the photoelectric response and plasticity linearity of the device by promoting rapid transfer of photogenerated holes and suppressing defect-trapping through a transient electric field. This study presents a low-cost, non-reconstructive, and environment friendly functional-recovery strategy, achieves the reactivation from the degradation condition of the synaptic devices, and offers a promising pathway toward stable and controllable neuromorphic hardware systems.

https://doi.org/10.1364/PRJ.601313

1. INTRODUCTION

In the era of artificial intelligence advancing toward brain-inspired computing, the development of neuromorphic devices with multi-perception and adaptive learning capabilities has emerged as a critical area of breakthrough [1,2]. Neuromorphic devices are designed to emulate the intricate functions of biological synapses or neurons, including precise responses to external stimuli and the capacity for adaptively modulating synaptic connections [3,4]. As one type of neuromorphic devices, photoelectric synapses have drawn substantial attention due to their potential to mimic the integrated "sensing-memory-learning" characteristics of the retina. Several materials, such as perovskite [5,6], 2D materials [7], vdW heterojunctions (BP/CdS [8], ZnO/graphene [9], and the like), and IGZO [10] have been employed as photon-sensitive materials to fabricate optical synapses. Among them, perovskites exhibit high photoelectric conversion efficiency [11,12], adjustable energy band structure [13], high carrier mobility [14], and remarkable defect tolerance [15], showing great potentials in perovskite-based X-ray detectors [16], photodetectors [17], and synaptic devices [18–20]. Long *et al.* demonstrated a bionic eye by using a hemispherical all-inorganic $CsPbI_3$ nanowire array that generates photocurrent without external bias, enabling a self-powered operating mode [18]. Yao *et al.* [19] and our group [20] showed that synaptic devices based on $CsPbBr_3$ perovskites effectively integrate light-sensing and synaptic functions, endowing memory devices with photo-programmable and electrically erasable features for image recognition.

Current research on these photoelectric synapses, including perovskite-based synaptic devices, primarily focuses on improving brain-inspired computing through optimization of synaptic functions (e.g., image recognition) and array integration. However, perovskite materials are highly susceptible to moisture-induced degradation in ambient conditions, which can trigger phase transitions and generate deep-level defects [21], resulting in a rapid decline in optoelectronic performance [22]. Although moisture-proof encapsulation techniques adapted from perovskite solar cells [23] offer partial protection against water vapor, device performance still gradually deteriorates over time due to aging of the encapsulation layers. To date, only research papers addressing the performance degradation repair of solar cells [24] and light-emitting diodes [25] have been published, and no studies on reactivating the performance of degraded perovskite synaptic devices have been reported yet. Therefore, developing a performance-oriented restoration strategy is essential to realize their practical potential.

Herein, to temporarily enhance the moisture resistance of perovskite [26] and suppress rapid phase transitions that lead to swift performance degradation, we fabricated an ion-gel-gated perovskite/graphene synaptic device using $TFSI^-$ anion-treated $CsPbBr_3$. After approximately one year of observation under natural moisture conditions, the photoelectronic response of such $CsPbBr_3$/graphene synaptic device degraded, leading to a decline in recognition accuracy from 96.13% to 67.8%. We propose a photoelectronic synergistic modulation strategy to restore optoelectronic response and enhance the linearity of long-term plasticity for eliminating the decline in recognition accuracy. This approach not only presents a viable functional-recovery mechanism but also establishes a foundation for future research on a closed-loop neuromorphic hardware with functional-recovery, underscoring its forward-looking perspective and innovative significance.

2. DEVICE STRUCTURE AND BASIC CHARACTERISTICS

Approximately 80% of external environmental information is perceived and acquired through the eyes, which play a crucial role in human life. The schema of eye and synapses are shown in Fig. 1(a). The retina consists of photoreceptors, as well as bipolar cells and ganglion cells that receive electrical neural signal stimulation. In this study, we selected halide perovskites as optoelectronic active materials for simulating artificial visual responses. Compared with other photovoltaic materials, e.g., oxides and chalcogenides, halide perovskites exhibit a favorable balance between material stability and high photoelectric conversion efficiency, making them particularly competitive.

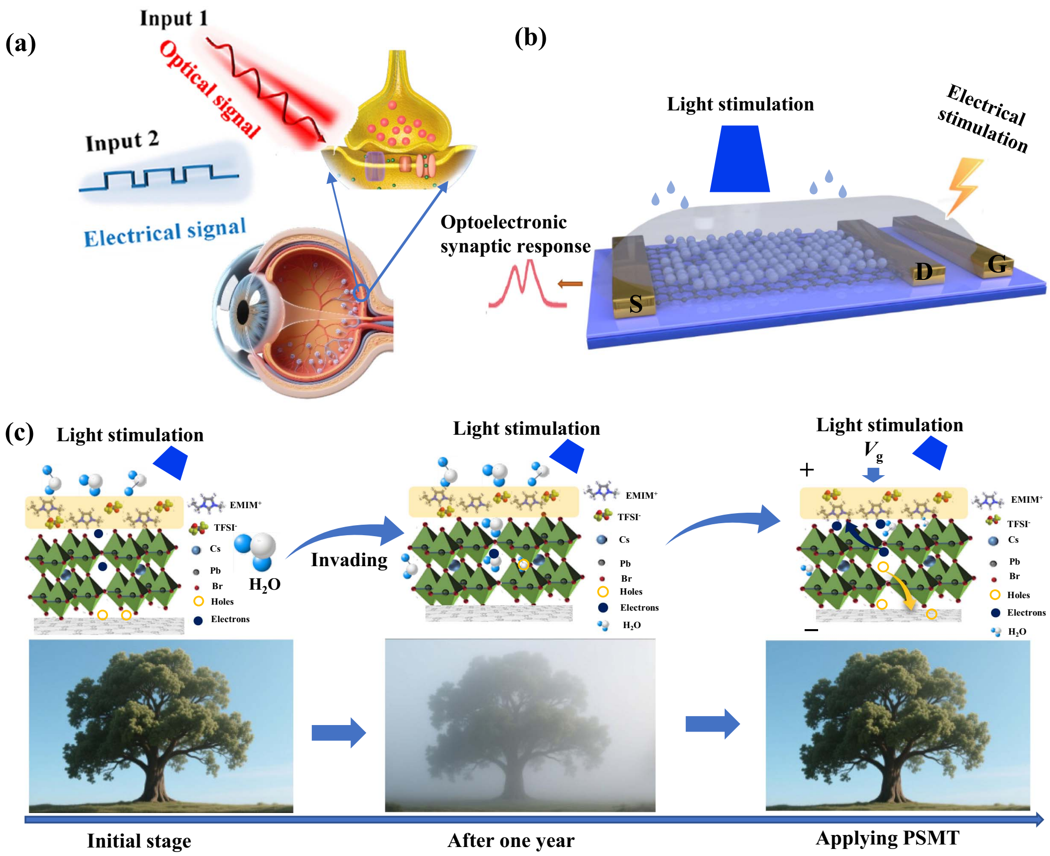

Fig. 1. Functional-recovery strategy of $CsPbBr_3$/graphene synaptic transistor. (a) Schematic illustration of the eye and synapses. (b) Schematic image of $CsPbBr_3$/graphene synaptic transistor. (c) Schematic illustration of the process and mechanism underlying its image recognition failure and functional-recovery.

We propose an ion-gel-gated $CsPbBr_3$/graphene synaptic transistor that enables both light perception and electrically stimulated response, as illustrated in Fig. 1(b). The channel layer of the device consists of a $CsPbBr_3$/graphene heterostructure, while the gate dielectric layer is composed of an ion gel. The source, drain, and gate electrodes are aligned in a linear configuration to facilitate effective modulation of channel carriers by the gate electric field generated through the ion gel. Au/Pd (50 nm/10 nm) electrodes of the gate-drain-source were fabricated on PI by sputtering and lithography technology. Wet-assisted single-layer graphene was transferred on the source and drain electrodes and PI substrate. The $CsPbBr_3$ nanocrystal solution was transferred onto a portion of the graphene film surface using dot-coating technology. Subsequently, the prepared ion gel solution with $EMIM^+$ cation and $TFSI^-$ anion was dropped on the $CsPbBr_3$ nanocrystal, graphene, and gate electrode by using the micro pipette for protecting the quantum dots. The ion gel is partially covering the graphene and gate electrode to realize the double-electric-layer property. Finally, the volatile solvent of the ion gel solution was removed with a hot plate at 100°C.

The schematic illustration of the process and mechanism underlying its image recognition failure and functional-recovery is presented in Fig. 1(c). Initially, $TFSI^-$ interacts with the uncoordinated lead ions (Pb^{2+}) and other defect sites on the perovskite surface, thereby anchoring to the surface. The enrichment of the -CF_3 group in the $TFSI^-$ anion forms a hydrophobic layer that effectively slows down water molecule penetration, thereby preventing rapid degradation of the perovskite phase [26]. At the initial state, such a synaptic transistor, functioning as a synapse, can be employed to construct a feed-forward neural network capable of achieving excellent image recognition performance. This unencapsulated device is exposed to the natural environment over the long term to simulate performance degradation scenarios that occur when encapsulation is inadequate or partially compromised. In a humid natural environment, H_2O gradually and slowly penetrated the perovskite layer, and prolonged exposure for over one year enhances ion migration and triggers phase transitions in the perovskite layer, leading to the formation of hydrated phases, e.g., $Cs_4PbBr_6 \cdot 2H_2O$ [27]. This degradation process generates additional deep-level defects and non-radiative recombination centers [26–28], thereby degrading the optoelectronic response and image recognition performance. Herein, a photoelectronic synergistic modulation technique (PSMT) is proposed and implemented in perovskite/graphene heterojunction synaptic transistors. PSMT dynamically couples pulsed gate voltage with concurrent light illumination to generate a transient interfacial electric field across the perovskite/graphene junction, exerting a directional force on photogenerated holes in the $CsPbBr_3$ layer and enabling their efficient transfer to the graphene channel while simultaneously suppressing defect-trapping, thereby enhancing image recognition performance. Crucially, PSMT operates as a functional-recovery strategy that temporarily circumvents defect-trapping pathways via field-assisted carrier extraction, other than altering the material structure or reverse phase degradation (e.g., transformation into $CsPb_2Br_5$ or hydrated phases).

Figure 2(a) shows the Raman spectrum of monolayer graphene, with the G-band and 2D-band wavenumbers at approximately 1582 cm^{-1} and 2706 cm^{-1}, respectively. The I_G/I_{2D} ratio of ~0.64 indicates that the graphene is p-type with some defects. To analyze the structural evolution of $CsPbBr_3$ after one year of natural environmental exposure, we performed

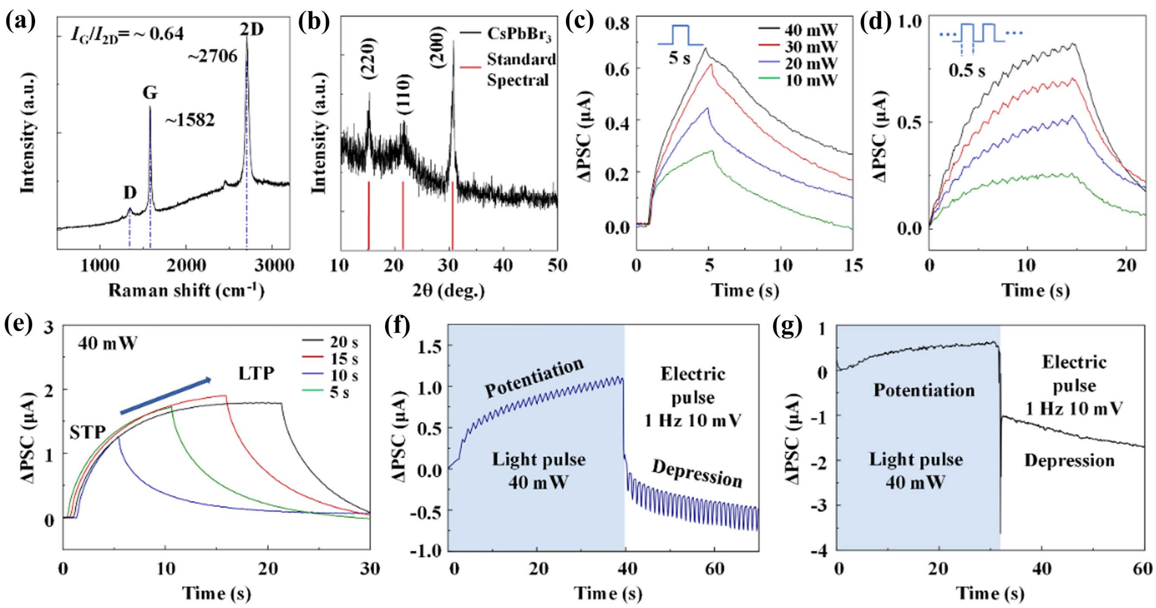

Fig. 2. Characterizations and performance of $CsPbBr_3$/graphene synaptic transistors. (a) Raman spectrum of the graphene. (b) XRD scanning schematic diagram of the $CsPbBr_3$ perovskite. (c) After performance degeneration, STP property under single-light-pulse stimulus. (d) After performance degeneration, LTP property under 15 consecutive light pulse stimuli. (e) Transition from STP to LTP due to light pulse duration change. (f) Initial data of the device about optic memory and electrical erasure. (g) Under natural environment over one year, the test data of the device about optic memory and electrical erasure.

X-ray diffraction (XRD) characterization following the material characterization method in Ref. [27] and obtained the corresponding diffraction patterns, as shown in Fig. 2(b). The crystal planes (220), (110), and (200) at 2θ angles of 14.8°, 21.8°, and 31°, respectively, were observed. The intensity of the main peaks at 14.8° and 21.8° is very weak, which is similar to the XRD spectrum in Ref. [27] after prolonged exposure to humidity (240 h), indicating that the perovskite phase of $CsPbBr_3$ material has undergone a transformation. This indicates that, although the $TFSI^-$-treated perovskite surface slows down water molecule penetration, prolonged exposure of the device to humidity can still allow gradual infiltration of water molecules, leading to partial degradation of the perovskite phase and the formation of a new crystalline phase, most likely a hydrate [27]. Prolonged exposure to ambient humidity induces a hydrated-phase transition in this intrinsically unstable $CsPbBr_3$ perovskite, generating deep-level trap states [21,28].

Synaptic plasticity, encompassing short-term synaptic plasticity (STP) and long-term synaptic plasticity (LTP), is fundamental to the ability of neurons and synapses to support regulatory, learning, and memory functions [29]. Through one year of continuous observation of long-term synaptic characteristics, it was found that the device did not exhibit significant degradation of its optoelectronic response until after one year. To further exhibit the degraded synaptic performance of the device after long-term moisture exposure, changes in post-synaptic current ΔPSCs under different light pulse stimuli are shown in Figs. 2(c)–2(e). In Fig. 2(c), with an increase of the light power from 10 to 40 mW, ΔPSCs increase from ~0.28 to ~0.75 μA. Subsequently, ΔPSCs associated with the LTP are presented in Fig. 2(d), which were obtained using 15 consecutive light pulses (pulse duration of 0.5 s, frequency of 1 Hz) with different light powers. With an increase of the light power, ΔPSCs increase from ~0.26 to ~0.87 μA. Another significant characteristic of synapses is the transition from STP to LTP. This transition is mimicked by modulating the duration of a single light pulse, as illustrated in Fig. 2(e). This transition behavior closely resembles that of biological synapses.

Prolonged exposure of the device to ambient air may adversely affect its long-term potentiation and depression. Figure 2(f) illustrates the initial photo-induced PSC response of the ion-gel-gated $CsPbBr_3$/graphene synaptic transistor under optical writing and electrical erasing. Figure 2(g) presents the test results obtained under the same conditions as those in Fig. 2(f) after one year of ambient storage. A comparison of the ΔPSC between Figs. 2(f) and 2(g) reveals that, under 30 consecutive light pulses (40 mW), the ΔPSC of the device decreased from ~0.92 μA in the initial state to ~0.66 μA after long-term ambient air exposure, corresponding to a degradation of approximately 28%, accompanied by waveform distortion and pronounced nonlinear behavior. The data shown in Figs. 2(f) and 2(g) are commonly used to extract synaptic weights for implementing learning and image recognition tasks.

To investigate its stability under long-term moisture exposure, photoelectric currents were measured under a 450 nm, 5 s light pulse stimulation, with comparative results shown at the initial stage and after one year of air exposure in Fig. 3. In Fig. 3(a), the maximal ΔPSC at the initial stage reaches ~0.92 μA. After one year, under the same conditions, the maximal ΔPSC decreases to about 0.75 μA, as shown in Fig. 3(b). This indicates that prolonged exposure to environmental water vapor reduces the device's optoelectronic response by approximately 18%, although there is no disruption of the synaptic plasticity for long-term operation. Inspired by the structure and function of the human retina, we further applied the ion-gel-gated $CsPbBr_3$/graphene synapse to perform letter "H" imaging with memory and forgetting processes. The resulting imaging matrices are presented in Figs. 3(c) and 3(d). During the second presentation of the letter "H" at the end of light stimulation, the recognition rate is observed to be slightly lower than in the initial test.

3. OPTOELECTRONIC SYNERGISTIC MODULATION RESULTS AND DISCUSSION

A stable control strategy is urgently required to reactivate performance-degraded synaptic devices caused by perovskite crystal structure changes [27] and to prevent photogenerated carriers from being captured by deep-level defect states [21,28]. It is well established that both the generation and collection of photogenerated carriers at the $CsPbBr_3$/graphene heterojunction are influenced by the external electric field. This understanding provides a promising avenue for developing a strategy to modulate the photocurrent behavior of these devices.

To elucidate the influence of an external electric field on photocurrent behavior, it is necessary to construct device band diagrams incorporating phase-change-induced deep-level defect states [28] related with XRD in Fig. 2(b), which aid in analyzing the transport mechanisms of photo-generated charge carriers, as shown in Figs. 4(a)–4(d). Without gate voltage, band bending occurs due to the Fermi level difference between the perovskite nanocrystal and graphene, resulting in the formation of a shallow potential barrier. The built-in electric field directs from the perovskite toward the graphene. Under illumination, the perovskite nanocrystal absorbs incident light energy and generates electron-hole pairs. Without an applied gate voltage, the built-in electric field is insufficient to drive photogenerated holes toward the graphene channel, resulting in deep-level defect-trapping of these carriers [28] and a reduction in the photocurrent. Under continuous high positive gate pulse stimulation, heterojunction band bending increases, thereby enhancing the transient built-in electric field. Under this strengthened transient electric field, photogenerated holes are effectively prevented from being trapped by the increased defect states within the perovskite and are rapidly transported to the graphene channel. Photogenerated electrons are trapped at the interface between the perovskite film and graphene due to the high potential barrier of the heterojunction. Consequently, the transfer of photogenerated holes to the graphene channel increases the p-doping level of the graphene, resulting in a downward shift of the graphene Fermi level and a corresponding increase in channel current, as illustrated in Figs. 4(e)–4(g). However, when a transient gate voltage of 12 mV is applied, photogenerated carriers are rapidly injected into the graphene

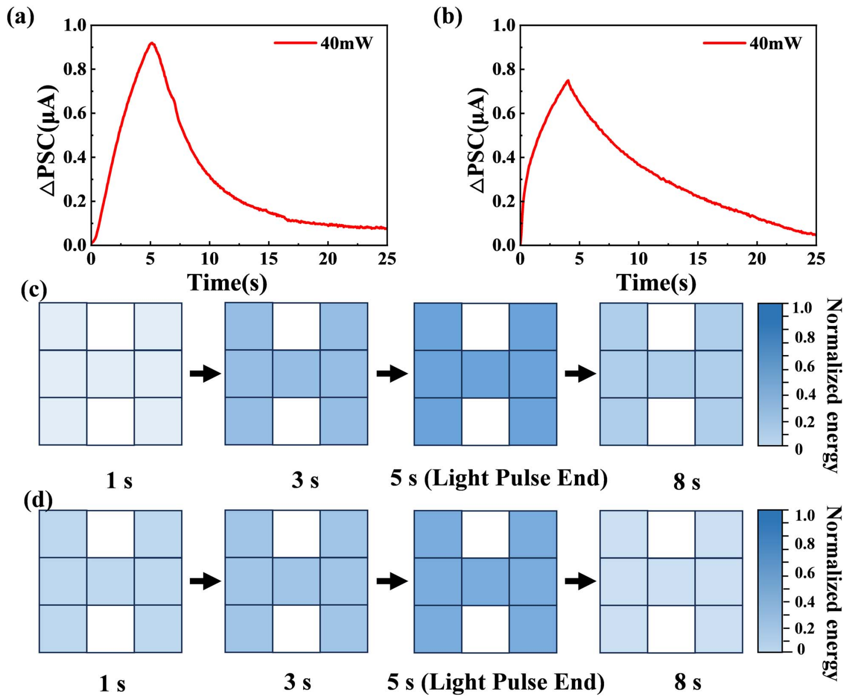

Fig. 3. Photocurrent and "H"-image memory changes over one year. (a) ΔPSC response of the initial test triggered by 5 s 450 nm light pulse with 40 mW optical power. (b) ΔPSC response of the second test triggered by 5 s 450 nm light pulse with 40 mW optical power under natural environment about one year. (c) Schematic diagram of light sensing matrix at the initial test. (d) Schematic diagram of light sensing matrix at the second test.

channel and quickly reach saturation. Subsequently, sustained electrical pulsing at 12 mV enables a small number of electrons to tunnel through the potential barrier into the graphene channel, causing a slight decrease in the saturated photocurrent and thereby enhancing the nonlinearity of the LTP response, as shown in Fig. 4(h). In summary, 10 mV is the optimal gate bias.

Based on the above-mentioned mechanism, PSMT has been incorporated into the device to modulate its photocurrent

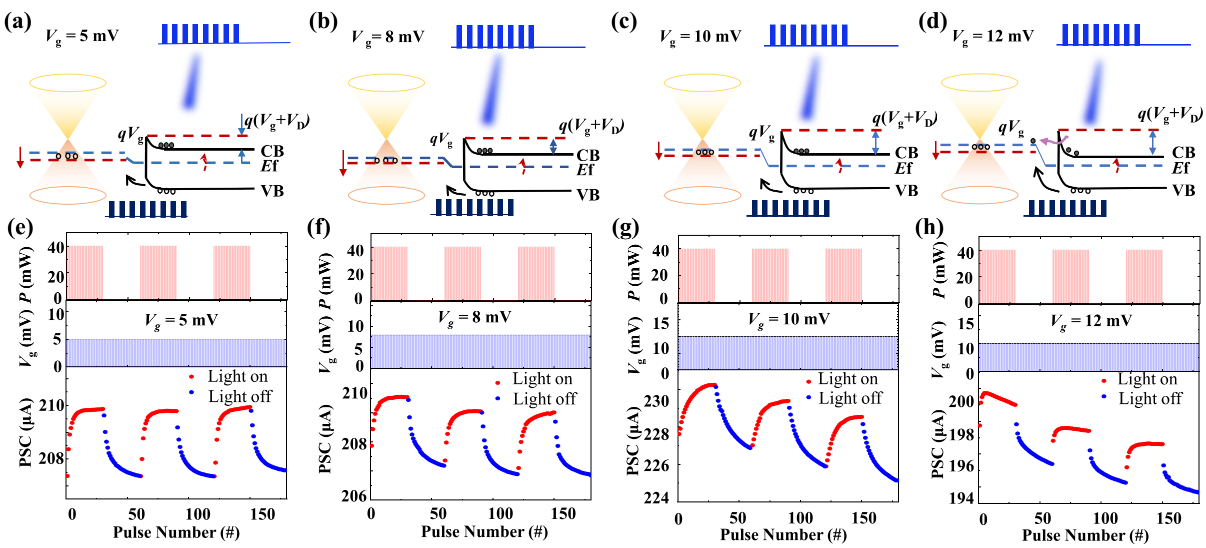

Fig. 4. Schematic diagram of heterojunction band structure under gate pulse voltage and test curves under PSMT. (a) Band structure under gate pulse voltage of 5 mV. (b) Band structure under gate pulse voltage of 8 mV. (c) Band structure under gate pulse voltage of 10 mV. (d) Band structure under gate pulse voltage of 12 mV. (e) Test curves of the devices with $V_{DS} = 0.05$ V, under photoelectric synergistic triggering induced by 500 ms light pulses (1 Hz, 40 mW) and 500 ms 1 Hz gate voltage pulses with $V_g = 5$ mV. (f) Test curves of the devices with $V_{DS} = 0.05$ V, under photoelectric synergistic triggering induced by 500 ms light pulses (1 Hz, 40 mW) and 500 ms 1 Hz gate voltage pulses with $V_g = 8$ mV. (g) Test curves of the devices with $V_{DS} = 0.05$ V, under photoelectric synergistic triggering induced by 500 ms light pulses (1 Hz, 40 mW) and 500 ms 1 Hz gate voltage pulses with $V_g = 10$ mV. (h) Test curves of the devices with $V_{DS} = 0.05$ V, under photoelectric synergistic triggering induced by 500 ms light pulses (1 Hz, 40 mW) and 500 ms 1 Hz gate voltage pulses with $V_g = 12$ mV.

behavior associated with long-term potentiation and depression, as illustrated in Figs. 4(e)–4(g). In one cycle shown in Fig. 4(e), a sequence of 30 consecutive light pulses (with pulse width of 500 ms, frequency of 1 Hz, and power of 40 mW) and continuous gate voltage pulses (1 s duration, 50% duty cycle, and 5 mV amplitude) synergistically stimulates the device under a drain-source voltage (V_{DS}) of 0.05 V, thereby inducing long-term potentiation. This process emulates the memory and learning process of the human retina. Following this, the termination of light pulses while maintaining the continuous 5 mV gate voltage pulses resulted in long-term depression, mimicking the forgetting process. Through repeated cycles that simulate both learning and forgetting processes, the PSC at the end of the third cycle is slightly higher than that of the beginning of the first cycle. The Ebbinghaus memory curve is successfully obtained from our device, as illustrated in Fig. 4(e). As the applied gate pulse voltage increases from 5 mV to 10 mV, the saturation tendency of the curves is reduced and the optoresponse currents and linearity are both improved. By comparing Fig. 4(e) with Fig. 4(g), it is observed that the photocurrent changes approximately 3.43 μA under 10 mV gate pulses, whereas under 5 mV it is approximately 2.56 μA. This indicates that the increase of the photocurrent associated with long-term potentiation is greater at 10 mV than at 5 mV, with a rise of nearly 34.8%.

An artificial neural network (ANN) is constructed for handwritten digit recognition due to our proposed synaptic transistors, as shown in Fig. 5(a). A three-layer perceptron-based BP neural network, serving as the ANN, with 784, 110, and 10 neurons in the input, hidden, and output layers, respectively, was adopted, in which the number of neurons in the input layer directly corresponds to the number of pixels in the MNIST images. Neurons in each layer transmit signals through synaptic weight connections and perform feature abstraction and pattern recognition using nonlinear activation functions, such as ReLU and sigmoid [30]. Synaptic weight updates are implemented by modulating the device conductance G in a crossbar switch array. To evaluate the nonlinearity N of test curves in Figs. 4(e)–4(g), the following formula [31], which relates to the normalized conductance G of the device, is used:

$$G(x) = \frac{G_{\max} - G_{\min}}{1 - \exp(-\alpha)} \left[1 - \exp\left(\frac{-\alpha}{P_{\max}} x \right) \right] + G_{\min}, \quad (1)$$

where $G_{\max}$, $G_{\min}$, and $P_{\max}$ are experimentally extracted parameters representing the maximum and minimum conductance values of the device, as well as the number of pulses

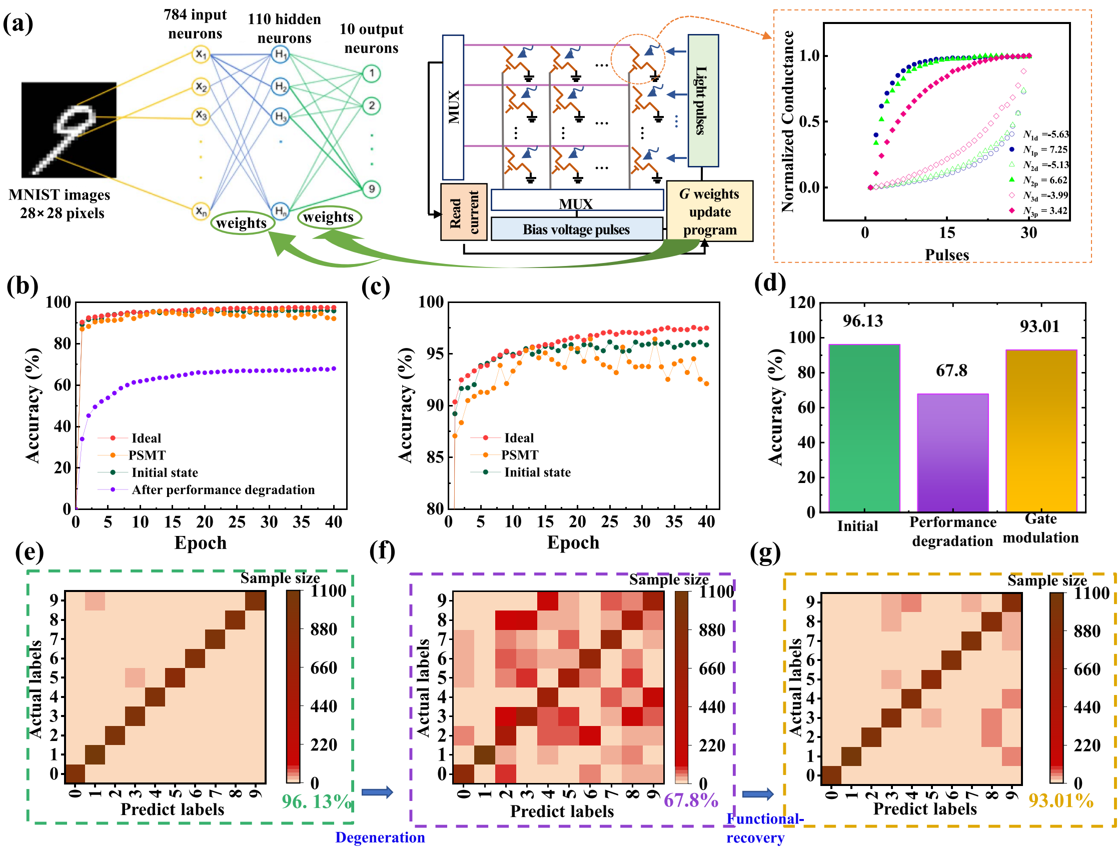

Fig. 5. Recognition of the optoelectronic synapse device array matrix. (a) Training diagram of the MNIST dataset for the ANN, and schematic diagram of the optoelectronic synapse device array matrix with synaptic weights update under PSMT with gate pulse voltages of 5 mV, 8 mV, and 10 mV. (b) Recognition accuracy associated with initial state, after degeneration, and under PSMT. (c) Enlarged view of the recognition accuracy associated with the initial state and PSMT compared to the ideal condition. (d) Comparison bar chart of final recognition accuracy. (e) Confusion matrix diagram of the device at initial state. (f) Confusion matrix diagram of the device over one year later under natural environment. (g) Confusion matrix diagram with the PSMT corresponding to gate pulse voltage of 10 mV.

required to switch between these conductance states. α is a fitting parameter that controls the normalized nonlinearity N of the weight update process [8]. The normalized conductance G and nonlinearities N_p and N_d of our device under gate pulse voltages of approximately 5 mV, 8 mV, and 10 mV are shown in Fig. 5(a). With the increase of the modulated gate-voltage, the nonlinearities are decreased. Especially, under 10 mV gate pulse voltage, N_{3p} and N_{3d} are approximately 3.42 and 3.99, respectively, which are lower than other gate pulse voltages.

It is worth noting that the ANN architecture employed in this study is highly simplified. The whole network was trained on the MNIST dataset, which consists of 28 × 28 pixel grayscale images of handwritten digits, including 60,000 training images and 10,000 test images. The MNIST dataset was used without any additional preprocessing, dimensionality reduction, filtering, or multi-stage feature extraction. Consequently, the recognition capability of the neural network is entirely determined by the intrinsic conductance modulation ability of the device and its synaptic plasticity. To further analyze the impact of changes in LTP over the one year on recognition performance, the recognition accuracies corresponding to the initial state, the degeneration state after one year, and PSMT are studied and presented in Figs. 5(b)–5(d). At the initial state, the recognition accuracy of the ANN is approximately 96.13%. After one year of exposure to natural environmental conditions, the accuracy decreases to 67.8% due to performance degradation. Under PSMT via light pulse and voltage pulse, the recognition accuracy reaches approximately 93.01%, representing a 3.12% reduction relative to the initial accuracy of 96.13%. This 3.12% reduction arises from perovskite crystal structure changes, which cannot be fully eliminated by functional-recovery strategies of the PSMT. This result indicates that PSMT exceeding 10 mV enhances the long-term potentiation of the device with respect to opto-response currents and improves the linearity of LTP, thereby enabling the neural network to recover its recognition accuracy to approximately 93.01%. It can not only be employed for device reactivation, but also lead to substantially low costs and consumption relative to strategies involving device re-fabrication, re-encapsulation, or replacement-processes that entail significant material, environmental, and economic costs.

We demonstrate the changes in recognition accuracy related to the initial state, after degeneration, and the PSMT using confusion matrices, as illustrated in Figs. 5(e)–5(g). In Fig. 5(e), each digit is clearly distinguishable, and the likelihood of misclassification is extremely low. Following device performance degradation, the confusion matrix in Fig. 5(f) reveals that the overall statistical recognition rate for handwritten digits is approximately 67.8%. By applying PSMT to this synaptic transistor, its simulation reorganization accuracy improved significantly, reaching 93.01%, with each digit clearly distinguishable in Fig. 5(g).

4. CONCLUSION

An ion-gel gated $CsPbBr_3$/graphene synaptic transistor was fabricated and demonstrated relatively stable operation for one year. After one year of exposure to the natural environment, ΔPSC associated with STP decreased from approximately 0.92 to 0.75 μA under stimulation by the same single-pulse light signal. Furthermore, this prolonged air exposure leads to degradation in LTP performance, accompanied by waveform distortion and pronounced nonlinear behavior, resulting in a significant decrease in recognition accuracy from 96.13% to 67.8%. A photoelectronic synergistic modulation technique is proposed to enhance the separation of photogenerated carriers in perovskite materials, prevent photogenerated holes from being trapped at internal defect states within the perovskite, and promote their rapid transfer to graphene, thereby facilitating efficient collection at the electrode. By increasing the modulated gate voltage from 5 mV to 10 mV, we observed reduced saturation tendency, improved linearity, and enhanced opto-current from approximately ~2.56 μA to ~3.43 μA, representing an ~34.8% increase, thus resulting in recognition accuracy from 67.8% to 93.01%, an absolute improvement of over 25%. This approach not only presents a functional-recovery strategy for degraded synaptic devices caused by increased defect states, highlighting its low-cost and reconstruction-free practical applicability, but also provides new insights into the future development of controllable brain-like neuromorphic computing systems.

Funding. National Natural Science Foundation of China (12474372, 62575023); State Key Laboratory of Information Photonics and Optical Communications (IPOC2025ZJ05, IPOC2024ZR01); Fundamental Research Funds for the Beijing University of Posts and Telecommunications (2025AI4S14); Beijing Nova Program from Beijing Municipal Science and Technology Commission (20230484433).

Disclosures. The authors declare no conflicts of interest.

Data Availability. Data underlying the results presented in this paper are not publicly available at this time but may be obtained from the corresponding authors upon reasonable request.

REFERENCES

1. G. Lee, J. H. Baek, F. Ren, *et al.*, "Artificial neuron and synapse devices based on 2D materials," Small **17**, 2100640 (2021).
2. N. Ilyas, J. Wang, C. Li, *et al.*, "Nanostructured materials and architectures for advanced optoelectronic synaptic devices," Adv. Funct. Mater. **32**, 2110976 (2022).
3. Y. Sun, J. Li, S. Li, *et al.*, "Advanced synaptic devices and their applications in biomimetic sensory neural system," Chip **2**, 100031 (2023).
4. M. Lee, H. S. Seung, J. I. Kwon, *et al.*, "Nanomaterial-based synaptic optoelectronic devices for in-sensor preprocessing of image data," ACS Omega **8**, 5209–5224 (2023).
5. Y. Wang, L. Yin, W. Huang, *et al.*, "Optoelectronic synaptic devices for neuromorphic computing," Adv. Intell. Syst. **3**, 2000099 (2021).
6. H. Jiang, H. Ji, Z. Ma, *et al.*, "Simultaneous achieving negative photoconductivity response and volatile resistive switching in Cs_2CoCl_4 single crystals towards artificial optoelectronic synapse," Light Sci. Appl. **13**, 316 (2024).
7. F. Tan, C. Chang, N. Zhang, *et al.*, "Physisorption-assistant optoelectronic synaptic transistors based on Ta_2NiSe_5/SnS_2 heterojunction from ultraviolet to near-infrared," Light Sci. Appl. **14**, 122 (2025).
8. C. Zhu, H. Liu, W. Wang, *et al.*, "Optical synaptic devices with ultra-low power consumption for neuromorphic computing," Light Sci. Appl. **11**, 337 (2022).

9. Z. Zhou, L. Wang, G. Liu, *et al.*, "A facile photonics reconfigurable memristor with dynamically allocated neurons and synapses functions," Light Sci. Appl. **14**, 269 (2025).
10. J. Sun, S. Oh, Y. Choi, *et al.*, "Optoelectronic synapse based on IGZO-alkylated graphene oxide hybrid structure," Adv. Funct. Mater. 1804397 (2018).
11. C. Liu, Y. Luo, R. Chen, *et al.*, "Graphene-perovskite composite structure facilitates high-performance X-ray detectors with low detection limits," Adv. Compos. Hybrid Mater. **9**, 34 (2026).
12. L. Zhang, H. Zhou, Y. Chen, *et al.*, "Spontaneous crystallization of strongly confined $CsSn_xPb_{1-x}I_3$ perovskite colloidal quantum dots at room temperature," Nat. Commun. **15**, 1609 (2024).
13. M. Saliba, T. Matsui, K. Domanski, *et al.*, "Incorporation of rubidium cations into perovskite solar cells improves photovoltaic performance," Science **354**, 206–209 (2016).
14. T. M. Brenner, D. A. Egger, L. Kronik, *et al.*, "Hybrid organic–inorganic perovskites: low-cost semiconductors with intriguing charge-transport properties," Nat. Rev. Mater. **1**, 15007 (2016).
15. W. Zhang, G. E. Eperon, and H. J. Snaith, "Metal halide perovskites for energy applications," Nat. Energy **1**, 16048 (2016).
16. W. Wu, J. Zhang, C. Liu, *et al.*, "Spontaneous cooling enables high-quality perovskite wafers for high-sensitivity X-ray detectors with a low-detection limit," Adv. Sci. **11**, 2410303 (2024).
17. Z. Gao, H. Zhou, K. Dong, *et al.*, "Defect passivation on lead-free $CsSnI_3$ perovskite nanowires enables high-performance photodetectors with ultra-high stability," Nano-Micro Lett. **14**, 215 (2022).
18. Z. Long, X. Qiu, C. L. J. Chan, *et al.*, "A neuromorphic bionic eye with filter-free color vision using hemispherical perovskite nanowire array retina," Nat. Commun. **14**, 1972 (2023).
19. Y. C. Yao, C. J. Lee, Y. J. Chen, *et al.*, "All-inorganic perovskite quantum-dot optical neuromorphic synapses for near-sensor colored image recognition," Adv. Sci. **12**, 2409933 (2025).
20. X. He, M. Xu, S. Liu, *et al.*, "Side ionic-gated perovskite/graphene heterojunction synaptic transistor with bipolar photoresponse for neuromorphic computing," Photonics Res. **12**, 1167–1174 (2024).
21. K. O. Ogunniran and N. T. Martins, "Humidity and moisture degradation of perovskite material in solar cells, effects on efficiency," IOP Conf. Ser. Earth Environ. Sci. **655**, 012049 (2021).
22. S. Dai, Y. Zhao, Y. Wang, *et al.*, "Recent advances in transistor-based artificial synapses," Adv. Funct. Mater. **29**, 1903700 (2019).
23. S. Ma, G. Yuan, Y. Zhang, *et al.*, "Development of encapsulation strategies towards the commercialization of perovskite solar cells," Energy Environ. Sci. **15**, 13–55 (2022).
24. M. Prete, M. V. Khenkin, D. Glowienka, *et al.*, "Bias-dependent dynamics of degradation and recovery in perovskite solar cells," ACS Appl. Energy Mater. **4**, 6562–6573 (2021).
25. P. Teng, S. Reichert, W. Xu, *et al.*, "Degradation and self-repairing in perovskite light-emitting diodes," Matter **4**, 3710–3724 (2021).
26. C. Tian, T. Wu, Y. Zhao, *et al.*, "Anion-stabilized precursor inks toward efficient and reproducible air-processed perovskite solar cells," Adv. Energy Mater. **14**, 2303666 (2024).
27. D. Di Girolamo, M. I. Dar, D. Dini, *et al.*, "Dual effect of humidity on cesium lead bromide: enhancement and degradation of perovskite films," J. Mater. Chem. A **7**, 12292–12302 (2019).
28. S. Cheng and H. Zhong, "What happens when halide perovskites meet with water?" J. Phys. Chem. Lett. **13**, 2281–2290 (2022).
29. A. Citri and R. C. Malenka, "Synaptic plasticity: multiple forms, functions, and mechanisms," Neuropsychopharmacology **33**, 18–41 (2008).
30. W. Shi, Z. Huang, H. Huang, *et al.*, "LOEN: lensless opto-electronic neural network empowered machine vision," Light Sci. Appl. **11**, 121 (2022).
31. C. Han, X. Han, J. Han, *et al.*, "Light-stimulated synaptic transistor with high PPF feature for artificial visual perception system application," Adv. Funct. Mater. **32**, 2113053 (2022).